

Thermal Upgrading of Nickeliferous Pyrrhotite Tailings for the Recovery of Nickel in the Form of Ferronickel Alloy



DAWEI YU, FENG LIU, JIAJING ZHANG, and MANSOOR BARATI

Production of ferronickel alloy by thermal treatment of nickeliferous pyrrhotite (Pyrr) tailings was studied by both thermodynamic assessment and experimentation. It was demonstrated that Ni can be extracted from Pyrr by increasing the Fe/S ratio of the material, which was achieved by either partial oxidation of Pyrr followed by H₂ reduction or *in situ* generation of metallic Fe from the reduction of magnetite by petroleum coke pre-mixed with Pyrr. Examination of the samples produced from thermal treatment at 1173 K demonstrated that both approaches were effective in generating ferronickel, although the size of the particles was suboptimal for subsequent separation. Increasing the ferronickel particle size could be achieved by a smelting step at 1473 K, forming a sulfur-deficient molten matte. Slow cooling of the molten matte resulted in precipitation, settling, and growth of ferronickel alloy particles.

<https://doi.org/10.1007/s11663-019-01646-5>

© The Minerals, Metals & Materials Society and ASM International 2019

I. INTRODUCTION

PYRRHOTITE (Pyrr, Fe_{1-x}S, $x = 0$ to 0.125) is ubiquitous in Ni-Cu sulfide ore deposits. In the beneficiation of Ni sulfide ores, the main Ni-bearing mineral, *i.e.*, pentlandite (Fe,Ni)₉S₈, is recovered into the Ni concentrate while the bulk of the sulfidic constituents being Pyrr is rejected as tailings to improve smelting capacity and minimize SO₂ emissions.^[1] It has been recognized that, for the Ni sulfide ores in the Sudbury region of Ontario, Canada, appreciable amounts of pentlandite occurs as micro-sized “flames” finely disseminated in the Pyrr matrix^[2]; as a consequence, this part of pentlandite together with Pyrr inevitably reports to the tailing stream. On the other hand, the non-stoichiometric Pyrr found in Sudbury has a dissolved Ni content in the range of 0.6 to 0.8 pct Ni, which represents more than half of the total Ni value contained in the Pyrr tailings.^[3] Estimates show that in Sudbury about 75 to 100 Mt Pyrr on a dry basis has been accumulated, and fresh Pyrr tailings are being produced

at a rate of up to ~ 5000 tpd.^[4] Given these facts, Sudbury Pyrr tailings may be regarded as a significant Ni resource, and a process for the recovery of Ni and mitigation of tailings has been of interest. Such a process could potentially be applied to Pyrr of other mines where there has been reports of high Ni contents, such as 2 to 3 pct Ni in Norilsk, Russia,^[5-7] and 1 to 2 pct Ni in Jinchuan, China.^[7,8]

The last attempt to commercially process Sudbury Pyrr tailings for value recovery was ended by Vale (formerly known as INCO) in 1991 with the shutdown of roasters.^[9] At present, impounding Pyrr tailings is practiced, which reportedly is the most effective measure to prevent the occurrence of acid mine drainage (AMD).^[10] However, subaqueous deposition of Pyrr tailings requires high maintenance costs, and the sulfide oxidation in Pyrr-rich tailing impoundments is an ongoing risk.^[11] In this regard, the development of economically sound and environmentally friendly technologies is still needed for processing of Sudbury Pyrr tailings to mitigate their long-term environmental impact.

A thermal upgrading process to concentrate Ni in an alloy phase followed by magnetic separation was first studied by Vale in the 1970s.^[12,13] The basic principle behind this process has been discussed in a previous publication.^[14] As shown in the Fe-Ni-S isotherm (Figure 1), at 1173 K, a monosulfide solid solution (mss) exists between Fe_{1-x}S and Ni_{1-x}S, and the Fe-rich portion of this ternary system is dominated by a two-phase assemblage “ γ + mss”. A typical composition of Sudbury Pyrr tailings^[15] indicated by a star symbol in Figure 1, is found to be located within the area of mss

DAWEI YU is with the School of Metallurgy and Environment, Central South University, 932 Lushan South Road, Changsha, Hunan 410083 P. R. China and also with the Department of Materials Science and Engineering, University of Toronto, 184 College Street, Toronto, ON M5S 3E4, Canada. Contact e-mail: dawei.yu@csu.edu.cn FENG LIU, JIAJING ZHANG, and MANSOOR BARATI are with the Department of Materials Science and Engineering, University of Toronto.

Manuscript submitted March 19, 2019.

Article published online July 23, 2019.

II. MATERIALS AND METHODS

A. Materials

The chemical composition of the as-received Pyrr tailing (dry-basis) is listed in Table I. As seen from its sulfur content, the Pyrr tailing is pure, containing 0.85 mass pct Ni with minor amounts of impurities such as Mg, Al, and Co. The particle size distribution of the as-received Pyrr tailing, determined by laser scattering, is shown in Figure 2(a) with a median particle size (*i.e.*, $d(0.5)$) of 26.1 μm . Figure 2(b) is the scanning electron microscope (SEM) image of the cross section of the Pyrr tailing. Energy-dispersive spectrometry (EDS) analysis on the cross section indicates the presence of minor amounts of magnetite particles, which explains the fact that the overall molar ratio of Fe:S is slightly higher than unity (Table I). The Pyrr tailing was initially dried at 378 K for 2 hours before use in the study.

Magnetite used in the study was in a fine powder form with 90 pct below 5.3 μm . Petroleum coke powder with a fixed carbon content of 85.1 mass pct was ground using a ball mill, and the fraction passing 38 μm sieve was used as the carbonaceous reductant.

B. Methods

1. Thermodynamic evaluation

Equilib module of the thermochemical software FactSageTM^[16] was employed to evaluate the influence of two most important parameters (*i.e.*, sulfur-to-metal ratio and temperature) on the phase evolution and compositions of the Fe-Ni-S system. Databases of FactPS and FTmisc were chosen for the evaluations. The first evaluation was performed by varying the molar ratio of S/(Fe + Ni) in the range of 0.25 to 1.0 at a temperature of 1173 K, while maintaining a constant Ni:Fe molar ratio of 0.0129, which is the same as that of the Pyrr tailing used in the investigation. The second evaluation was conducted at temperatures ranging from 773 K to 1473 K at a S/(Fe + Ni) molar ratio of 0.7 and a Ni:Fe molar ratio of 0.0129, to study the influence of temperature on the formation of metallic phase when sulfur is deficient in the Fe-Ni-S system.

2. Thermogravimetric analysis

Thermogravimetric analysis (TGA) and differential thermal analysis (DTA) were performed using a Setaram TG-DTA 92 unit (SETARAM Inc., Newark, CA), which was coupled with a gas analyzer (ABB EL3020) for continuous analysis of the CO, CO₂, and/or SO₂ concentrations in the offgas. To determine the appropriate temperature for the partial oxidation of Pyrr, it is of great importance to first determine the oxidative reaction sequence of Pyrr by air as a function of reaction temperature. This was examined by heating a 10-mg Pyrr sample, which was placed loosely inside an alumina crucible (I.D. 7.2 mm) in the TGA unit at a heating rate of 10 K/min to 1283 K with an air flowrate of 500 mL/min. Individual samples were collected after reaching a particular intermediate temperature by moving the sample to the cold end of the TGA heating chamber,

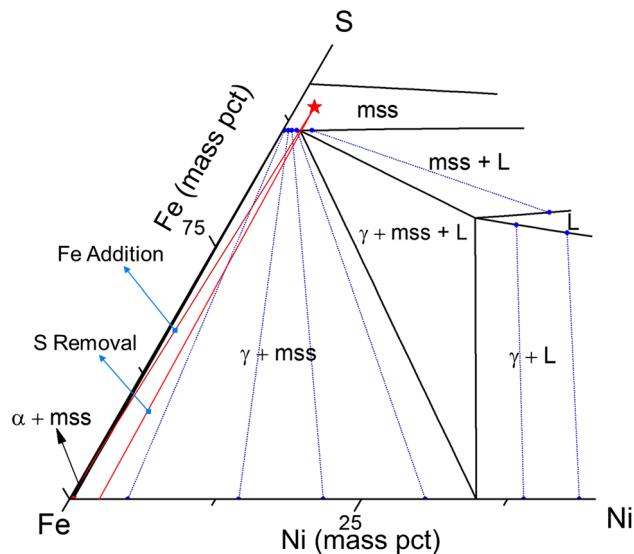


Fig. 1—Fe-rich portion of the Fe-Ni-S system at 1173 K, illustrating the basic principle of the thermal upgrading process.^[16]

and close to the Fe-S side. The thermal upgrading process can be viewed as the change in phase associations from a one-phase region “mss” to a two-phase region or even a three-phase region “alloy + mss” as a result of the modification in the overall composition. This can be achieved by adding iron into and/or removing sulfur from the Pyrr lattice, thereby converting nickeliferous Pyrr to a mixture of FeNi alloy and sulfide phases. The possibility of extracting Ni from nickeliferous Pyrr, thus, relies on its significantly higher solubility in γ than in mss, which is thermodynamically determined by the position of tie lines in “ γ + mss”. Therefore, the main function of the thermal upgrading process would be to increase the Fe/S ratio of the system to approach stoichiometric iron sulfide, FeS.

In this study, a thermodynamic assessment of the thermal upgrading process was performed using the thermochemical software FactSageTM.^[16] Narrowing down the range of favorable conditions, two experimental approaches were then employed to increase the Fe/S molar ratio of the Pyrr tailings. The first approach was the removal of sulfur by partial oxidation of Pyrr with air. Oxidation inevitably introduces oxygen in the form of iron oxides, necessitating the subsequent reduction of the oxide. Hydrogen (H₂) was used as the reductant for this reduction. The second approach was the addition of iron (Figure 1), which was realized by mixing Pyrr with magnetite (Fe₃O₄) and a carbonaceous reductant. During the pyrometallurgical treatment process, metallic Fe was formed *in situ* from the direct reduction of Fe₃O₄ with carbon. The overall objectives of this study are (1) to gain a better understanding of the thermal upgrading process from the perspectives of both reaction mechanisms and kinetics, and (2) to promote the growth of ferronickel alloy particles, facilitating their subsequent separation from the residual sulfides.

thereby allowing the sample to be air-quenched. These intermediate samples were subjected to both SEM and X-ray powder diffraction (XRD) analyses.

Sequential partial oxidation-reduction of the Pyrr sample (10 mg) was performed by initially heating in an Ar flow of 500 mL/min at 15 K/min to the predetermined oxidation temperature, and holding at this temperature for 15 min. During this dwelling time, purging gas was switched to air (extra dry, 500 mL/min) for a short time (15 or 25 seconds), achieving partial oxidation. The sample was subsequently heated to a higher temperature of 1173 K in Ar (grade 5.0 N, 500 mL/min) at 15 K/min, and holding at this temperature for 2 hours before cooling to room temperature. During this dwelling time, purging gas was switched to a N₂-15 vol pct H₂ gas for a determined period of time, allowing subsequent reduction. After cooling in Ar to room temperature, the samples were analyzed by SEM/EDS.

Heating of the mixtures of Pyrr, magnetite, and petroleum coke was conducted using a sample pellet. Pyrr, magnetite, and petroleum coke were mixed thoroughly at a mass ratio of 3.0:1.0:0.4, resulting in the pellet composition of 68.2 mass pct Pyrr, 22.7 mass pct magnetite, and 9.1 mass pct petroleum coke. A sample mixture of typically 30 mg was placed inside a 10-mm die set and pressed to form a pellet using a hydraulic press with a pressure of approximately 600 MPa. The pellet was broken to form three to five pieces of fragments before placing into the alumina crucible (I.D. 7.2 mm) for thermal treatment in the TG-DTA unit, with a continuous Ar flow of 500 mL/min.

In all the TGA experiments, the microbalance chamber of the unit was continuously purged with an isolating Ar gas stream of 7 mL/min to protect the microbalance. This Ar gas subsequently enters the heating chamber, causing slight dilution of the main reaction gas.

3. SEM and XRD analyses

Polished sections of the thermally treated samples were prepared by mounting the samples into epoxy resin, which were subsequently ground using silicon carbide papers in a dry condition and polished using the mineral oil-based, 1- μ m diamond suspension, thereby preventing the possible loss of water-soluble phases (*e.g.*, sulphates) from the sample during sample preparation. Polished sections were examined by SEM (JEOL, JSM-840), complemented by an EDS (PGT/AAT), using an accelerating voltage of 20 kV. For XRD analysis, the samples were manually ground using a mortar and pestle, which were then mixed with acetone on a single crystalline silica slide for analysis. XRD spectra were then acquired on a Philips PW2273/20 diffractometer using Cu K α radiation.

III. RESULTS AND DISCUSSION

A. Thermodynamic Evaluation

According to the Fe-Ni-S isotherm at 1173 K shown in Figure 1, formation of the γ alloy phase is dependent on the degree of sulfur deficiency in terms of the sulfur-to-metal (Fe + Ni) molar ratio. Figure 3(a) shows the results of thermodynamic evaluation with the Fe/S ratio as the variable. In the figure, $\frac{\text{Ni in } \gamma}{\text{Ni} - \text{total}}$ represents the Ni recovery into the γ phase, $\frac{\gamma}{\gamma + \text{Pyrr}}$ represents the mass pct of the γ phase in the product after reaching thermodynamic equilibrium, and $\frac{\text{Ni}}{\text{Fe} + \text{Ni}}$ in γ represents the Ni concentration (wt pct) in the γ phase (*i.e.*, highest

Table I. Elemental Composition (Mass Percent) of the Pyrr Tailing (Dry-Basis)

Elements	Fe	S	Ni	Cu	Mg	Al	Co
Mass Percent	62.86	35.66	0.85	0.16	0.15	0.03	0.01

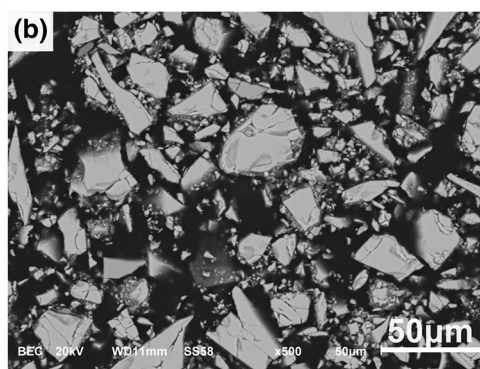
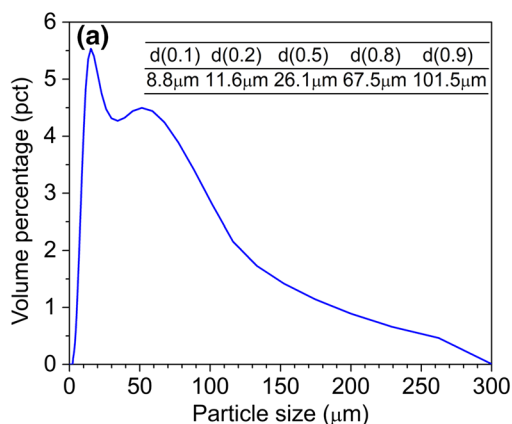


Fig. 2—Particle size distribution (a) and cross-sectional microscopical image (b) of the Pyrr tailing.

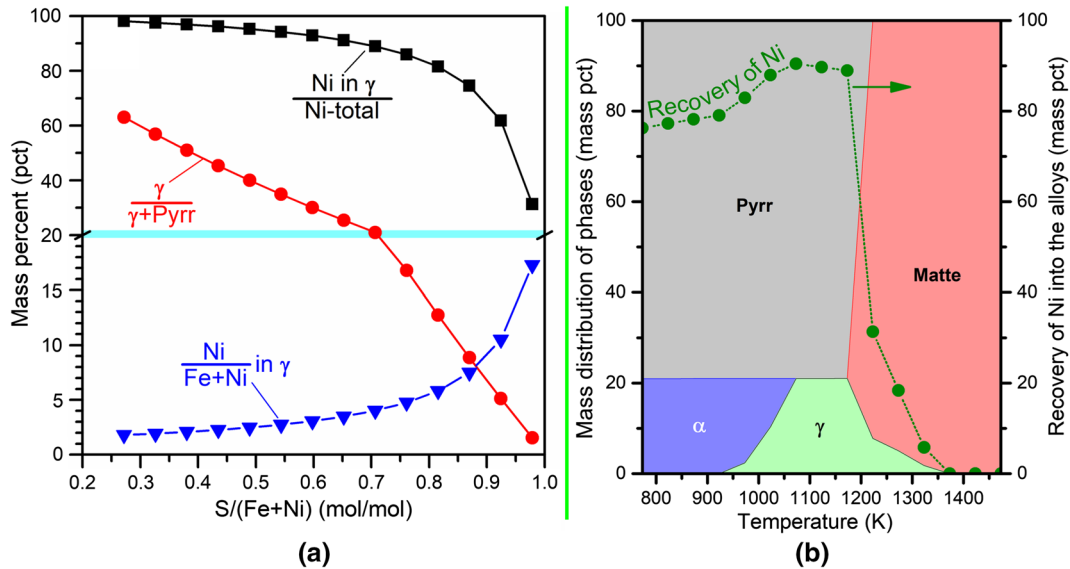


Fig. 3—FactSage™ simulation on (a) the effect of the molar ratio of S/(Fe+Ni) on the formation of γ alloy phase at 1173 K. (The horizontal line indicates the change in the scale of γ -axis.) (b) The effect of temperature on the formation of various phases and the degree of Ni recovery into the alloys.

possible Ni grade in the FeNi product). As seen, Ni recovery into the γ phase can be increased with a higher sulfur deficiency, which will result in a lower Ni concentration in the γ phase. For example, by reducing the sulfur-to-metal ratio from 0.92 to 0.76, Ni recovery can be increased from 62 to 86 pct accordingly, but the Ni concentration in the γ phase decreases from 10.5 to 4.8 mass pct. Therefore, the degree of sulfur deficiency should be optimized to achieve a relatively high degree of Ni recovery while having an acceptable Ni grade in the alloy.

The influence of temperature on the formation of various phases and on the recovery of Ni into the alloys (*i.e.*, $\frac{\text{Mass of Ni in alloys}}{\text{Mass of Ni in total}} \times 100\text{pct}$) was also evaluated, which is presented in Figure 3(b). As seen, with the increase of temperature in the range of 923 K to 1073 K, alloy isomorphous phase transformation from α to γ takes place, which also leads to an increase in the Ni recovery by approximately 10 pct. Temperatures higher than 1173 K lead to the formation of a Ni-bearing molten matte phase, which drastically reduces the formation of alloy phase(s) as well as Ni recovery. Therefore, the optimal temperature for Ni recovery into the alloy phase should be in the range of 1073 K to 1173 K.

B. Thermal Oxidation of Pyrr

To allow the determination of an appropriate temperature for the partial oxidation of Pyrr, the oxidation reaction sequence of Pyrr was deduced based on TG/DTA analysis. Figure 4 shows the TG, DTG, DTA, and offgas SO_2 concentration plots against temperature. Occurrence of a thermal event would be reflected by the change in mass (TG or DTG) and/or heat flow (DTA). Determination of the nature of the thermal event can be

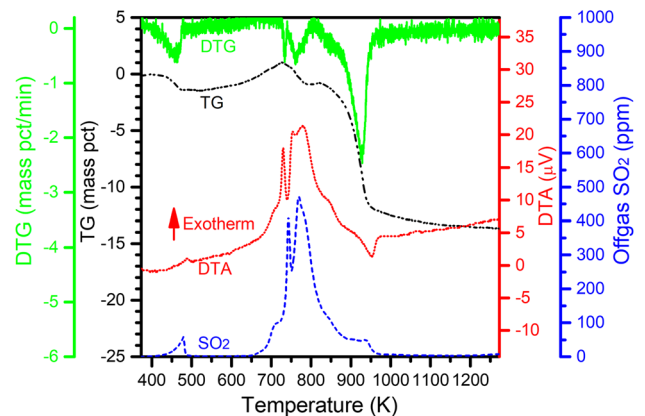


Fig. 4—TG/DTA and offgas analyses for the continuous heating of the Pyrr tailing at 10 K/min in an air flow of 500 mL/min.

achieved by coupling the TG/DTA results with the analysis on the intermediate products collected before and right after the thermal event, using XRD (Figure 5) and SEM (Figure 6).

The first thermal event took place in the temperature range of 413 K to 474 K, resulting in a slight mass loss by approximately 1.4 mass pct and SO_2 evolution. DTA curve indicates that a corresponding exotherm took place at this temperature range. The XRD analysis on the intermediate product samples collected from 474 K (Figure 5) suggests the formation of $\epsilon\text{-Fe}_2\text{O}_3$, which shows that this exotherm should be the surface oxidation of Pyrr, represented by Reaction [1] in Table II. Being one of the four polymorphs of iron (III) oxide, $\epsilon\text{-Fe}_2\text{O}_3$ is orthorhombic with crystallographic group $Pna2_1$.^[17] This less common polymorph transformed into the more common $\alpha\text{-Fe}_2\text{O}_3$ (Reaction [2] in

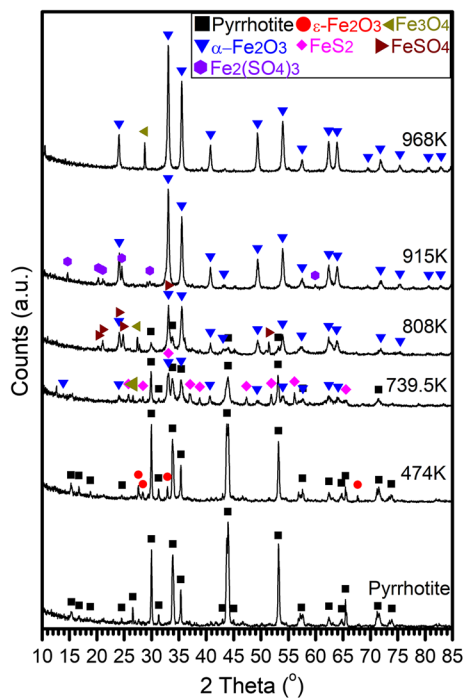


Fig. 5—XRD patterns for the Pyrr tailing and intermediate products collected from various temperatures.

Table II) in the temperature range of 474 K to 739 K, based on the XRD results (Figure 5). In the temperature range of 474 K to 739 K, a gradual mass gain took place, which was likely due to the occurrence of Reaction [3]. Considering this reaction is based on the presence of significant amounts of both α -Fe₂O₃ and pyrite (FeS₂) in the intermediate products from 739.5 K, as shown in Figures 5 and 6(c). A partially overlapped thermal event also took place, leading to the evolution of SO₂ at temperatures higher than 653 K. This exotherm is due to the oxidation of Pyrr forming α -Fe₂O₃ (Reaction [4]). This reaction extended to temperatures as high as 915 K, leading to the gradual development of a typical columnar structure of the formed Fe₂O₃ as shown in Figures 6(d) and (e). Formation of this characteristic columnar structure was due to the preferential inward oxidation along certain crystallographic planes.^[18–20] In the temperature range of 739 K to 808 K, oxidation of FeS₂ took place (*i.e.*, Reaction [5]), evidenced by the disappearance of FeS₂ peaks in the XRD pattern at 808 K (Figure 5), as well as the quick evolution of SO₂ and mass loss in this temperature range as shown in Figure 4. The partial pressure of SO₂ within the sample bed was high due to the quick evolution of SO₂ in the temperature range of 739 K to 915 K, which favored the formation of sulfates.^[18] As a result, a layer of FeSO₄ or Fe₂(SO₄)₃ formed on the surface of partially oxidized Pyrr particles (Figures 6(d) and (e)), which can be represented by Reactions [6] and [7]. Thermal decomposition of the sulfate at 915 K to 968 K took place, leading to the quick mass loss (Figure 4) and disappearance of the sulfate phase at 968 K (Figures 5 and 6(f)).

C. Sequential Partial Oxidation–Reduction of Pyrr

From the study on the oxidation reaction sequence of Pyrr (Section III–B), it is seen that the principal oxidation reaction that leads to sulfur removal is Reaction [4], which spans over a wide temperature range from 653 K to 915 K. Therefore, partial oxidation of Pyrr was performed at the temperature of 873 K. After oxidation at 873 K for 25 seconds in the TGA unit, Fe₂O₃ having its characteristic columnar structure was formed in the outer portion of Pyrr particles, based on the SEM analysis. From the mass loss during oxidation, it was estimated that the degree of sulfur removal was approximately 35 pct.

The partial oxidation–reduction test (Test R1) was therefore performed by oxidation at 873 K for 25 seconds followed by H₂ reduction at 1173 K for 7200 seconds (Figure 7). As seen from Figure 7, a quick mass loss took place after exposure to air at 873 K, indicating an extremely high oxidation rate. Two distinct stages are apparent during reduction at 1173 K based on the TG curve. Lasting for approximately 150 seconds, the first stage is characteristic of a high reduction rate, reflected by the quick mass loss. This fast reduction stage should be the reduction of oxide that was formed during the initial oxidation step because H₂ reduction of iron oxides is generally fast at 1173 K.^[21] In contrast, the second stage exhibits a relatively linear and much slower mass loss rate. The mass loss reached 32.4 mass pct after reduction for 7200 seconds, representing approximately 79 pct sulfur removal. This means sulfur was further removed during the second reduction stage by about 44 pct, in addition to the 35 pct sulfur removal during the initial oxidation. This points to the direct reduction of sulfide by H₂, *i.e.*, Reaction [9]. The slow kinetics of the second reduction stage was possibly due to its small thermodynamic equilibrium constant ($K = 4.2 \times 10^{-3}$ at 1173 K^[16]). According to Kor,^[22] the slow rate of hydrogen reduction of pyrrhite at a temperature range of 873 to 1173 K was mainly controlled by the counter-current diffusion of H₂ and H₂S in the gas-film boundary layer and in the porous iron layer. Figure 8 exhibits the cross section of the reduced product from Test R1, showing the presence of two major phases: alloy and sulfide. EDS point analysis along the arrow (Figure 8(b)) indicates that the Ni concentration in the sulfide phase was below the detection limit and that Ni became highly concentrated into the alloy phase. The mechanism that governs the migration of Ni into the alloy phase was the difference of the thermodynamic equilibrium Ni concentration in the sulfide *vs* alloy phases.^[14] In the alloy region, Ni concentration was higher as it was further away from the sulfide/alloy boundary, up to 13 mass pct. Based on the observation, Ni can be successfully concentrated into the alloy during H₂ reduction, allowing for further Ni recovery. However, due to the excessive reduction of sulfide by H₂ (Reaction [9]), the mass ratio of alloy to sulfide in the product was approximately 2.4:1, resulting in a much lower average Ni grade of the alloy (*i.e.*, the Ni concentration).

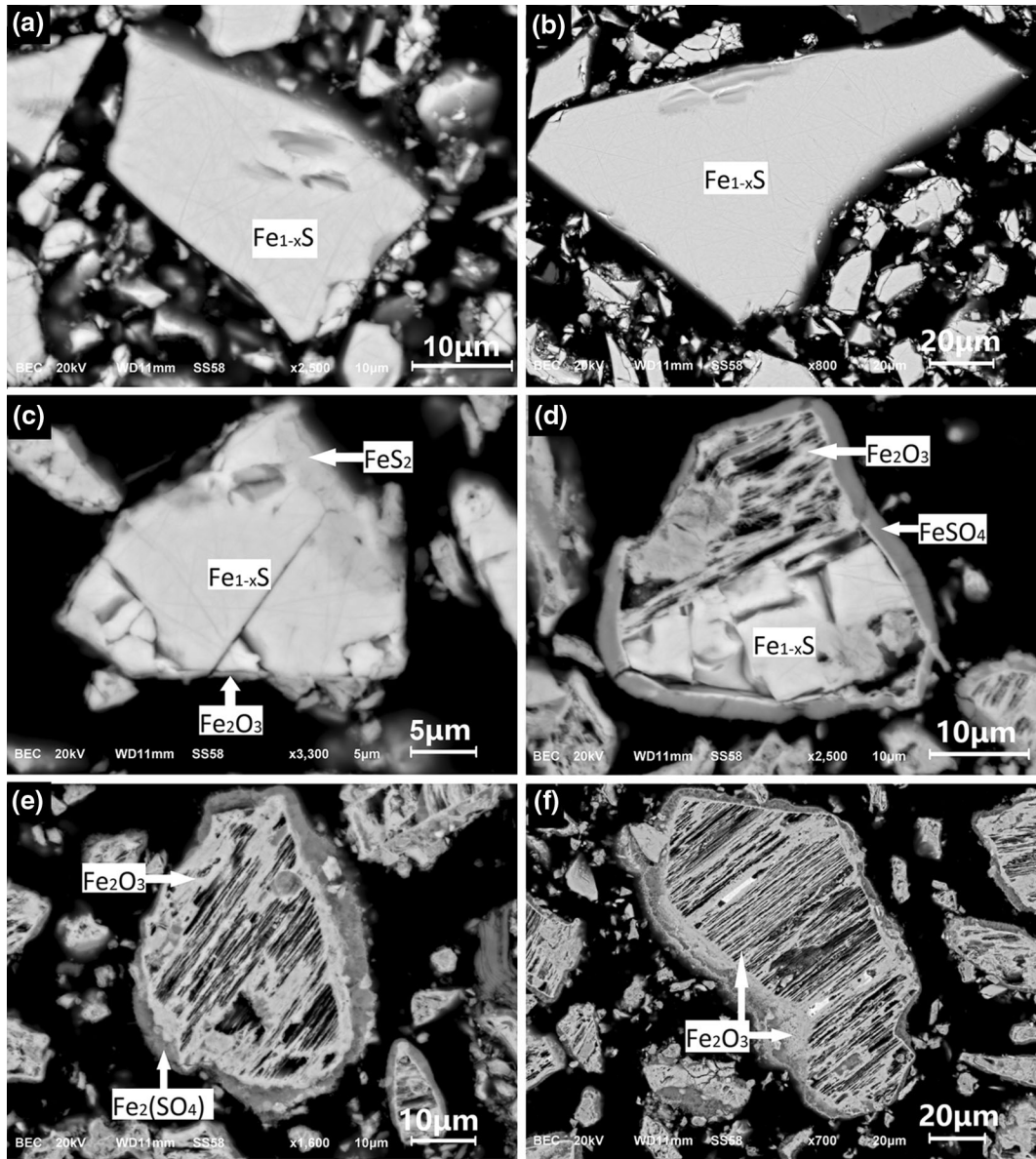
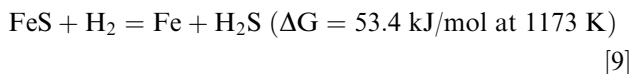


Fig. 6—Backscattered scanning electron (BSE) micrographs of the (a) Pyrr tailing and intermediate products collected from various temperatures (b: 474 K; c: 739.5 K; d: 808 K; e: 915 K; f: 968 K).

Table II. Deduced Reaction Sequence During the Thermal Oxidation of Pyrr

Temperature Range	Reactions	Reaction Number
413 K to 474 K	$2\text{Fe}_{1-x}\text{S} + (3.5 - 1.5x)\text{O}_2 = (1 - x)\varepsilon\text{-Fe}_2\text{O}_3 + 2\text{SO}_2$	(1)
474 K to 739 K	$\varepsilon\text{-Fe}_2\text{O}_3 = \alpha\text{-Fe}_2\text{O}_3$	(2)
474 K to 739 K	$2\text{Fe}_{1-x}\text{S} + (0.75 - 1.5x)\text{O}_2 = (0.5 - x)\alpha\text{-Fe}_2\text{O}_3 + \text{FeS}_2$	(3)
653 K to 915 K	$2\text{Fe}_{1-x}\text{S} + (3.5 - 1.5x)\text{O}_2 = (1 - x)\alpha\text{-Fe}_2\text{O}_3 + 2\text{SO}_2$	(4)
739 K to 808 K	$2\text{FeS}_2 + 5.5\text{O}_2 = \alpha\text{-Fe}_2\text{O}_3 + 4\text{SO}_2$	(5)
739 K to 808 K	$\text{Fe}_{1-x}\text{S} + (2 - x)\text{O}_2 = (1 - x)\text{FeSO}_4 + x\text{SO}_2$	(6)
808 K to 915 K	$2\text{FeSO}_4 + \text{SO}_2 + \text{O}_2 = \text{Fe}_2(\text{SO}_4)_3$	(7)
915 K to 968 K	$\text{Fe}_2(\text{SO}_4)_3 = \alpha\text{-Fe}_2\text{O}_3 + 3\text{SO}_2 + 1.5\text{O}_2$	(8)



A second test (Test R2, Figure 7) was therefore performed by allowing the reduction stage for only 150 seconds, which prevented the remaining sulfide from the excessive H₂ reduction, Reaction [9]. This resulted in a much lower alloy to sulfide mass ratio of the product, which was estimated to be 0.34:1. As seen from Figure 9(a), indeed much lower amounts of alloy phase were produced compared with Test R1 (Figure 8(a)). Essentially all alloy phases were intimately attached to the sulfide particles, enabling the possible Ni diffusion from sulfide to alloy. Figure 9b exhibits a Pyrr particle with few alloy particles at the edge of sulfide, measuring < 10 μm. EDS point analysis along the arrow crossing the alloy/sulfide phase boundary is plotted in Figure 9(c). As seen, Ni concentration of the sulfide phase was lowered from an average 0.85 mass pct before thermal treatment to an undetectable level, and the alloy

particles were highly concentrated with Ni with a concentration gradient from approximately 5 to 12 mass pct. Ni was therefore upgraded in the form of ferronickel alloy by a factor of about 10.

A third thermal treatment test (Test R3) was also performed at an even smaller degree of sulfur removal by oxidation. As seen from Figure 7, oxidation was conducted for only 15 seconds, as opposed to 25 seconds used for the other two tests. This resulted in a lower degree of sulfur removal at 23 mass pct, compared with 35 mass pct for Test R2. The amount of iron oxides produced apparently required a shorter time for subsequent reduction, which was about 116 seconds (Figure 7). Figures 9(d) through (g) illustrate the cross sectional micrograph of the product and its elemental mapping. Similarly, Ni became highly concentrated into the ferronickel alloy, demonstrating the effectiveness of the thermal treatment in terms of upgrading and recovery of Ni.

D. Thermal Treatment on Mixtures of Pyrr, Magnetite, and Petroleum Coke

Pellet fragments composed of 68.2 mass pct Pyrr, 22.7 mass pct magnetite, and 9.1 mass pct petroleum coke were thermally treated in Ar at 1173 K for 30 minutes (Test T1). As seen from Figure 10, two SO₂ peaks appeared in the temperature range of 473 K to 973 K, leading to a mass loss of approximately 4 mass pct. This was likely resulting from the reaction(s) between Pyrr and magnetite. Reduction of magnetite by petroleum coke (Reactions [10] and [11]) took place at temperatures above 973 K, evidenced by the evolution of both CO and CO₂ gases and its corresponding mass loss. SEM analysis of the thermally treated product (Figure 11) revealed the formation of ferronickel alloy particles with sizes smaller than 10 μm. EDS analysis on selected alloy particles indicates the presence of 13 to 21 mass pct Ni, owing to the Ni diffusion from the nickeliferous sulfide to the newly formed metallic Fe by the reduction of magnetite. However, the sulfide phase still contained 0.35 to 0.45 mass pct Ni, indicating that

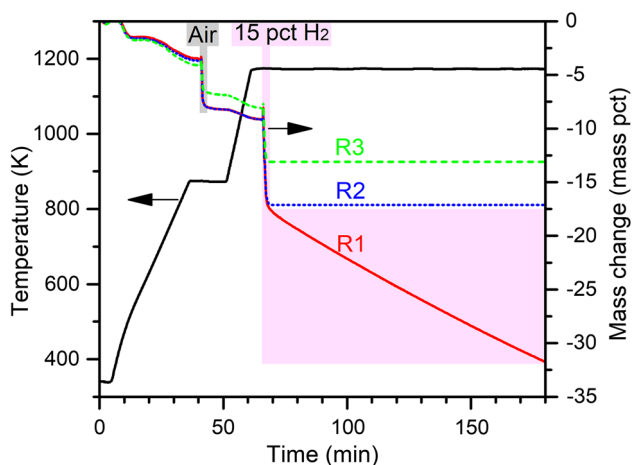


Fig. 7—TGA partial oxidation of Pyrr at 873 K followed by H₂ reduction at 1173 K (R1: oxidation for 25 s, reduction for 7200 s; R2: oxidation for 25 s, reduction for 150 s; R3: oxidation for 15 s, reduction for 116 s).

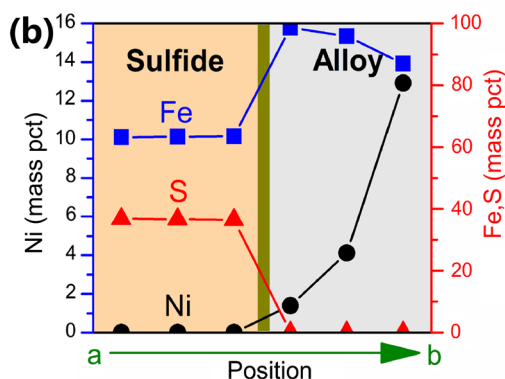
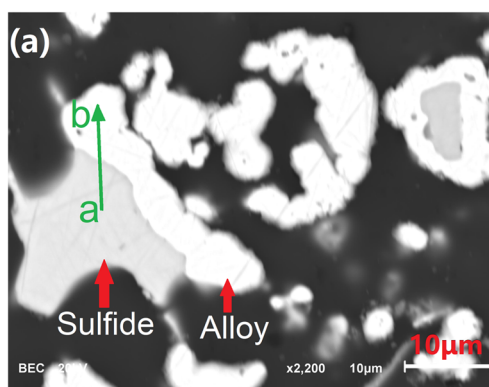


Fig. 8—(a) BSE micrograph of the reduced product from Test R1, and (b) EDS point analysis along the arrow a → b.

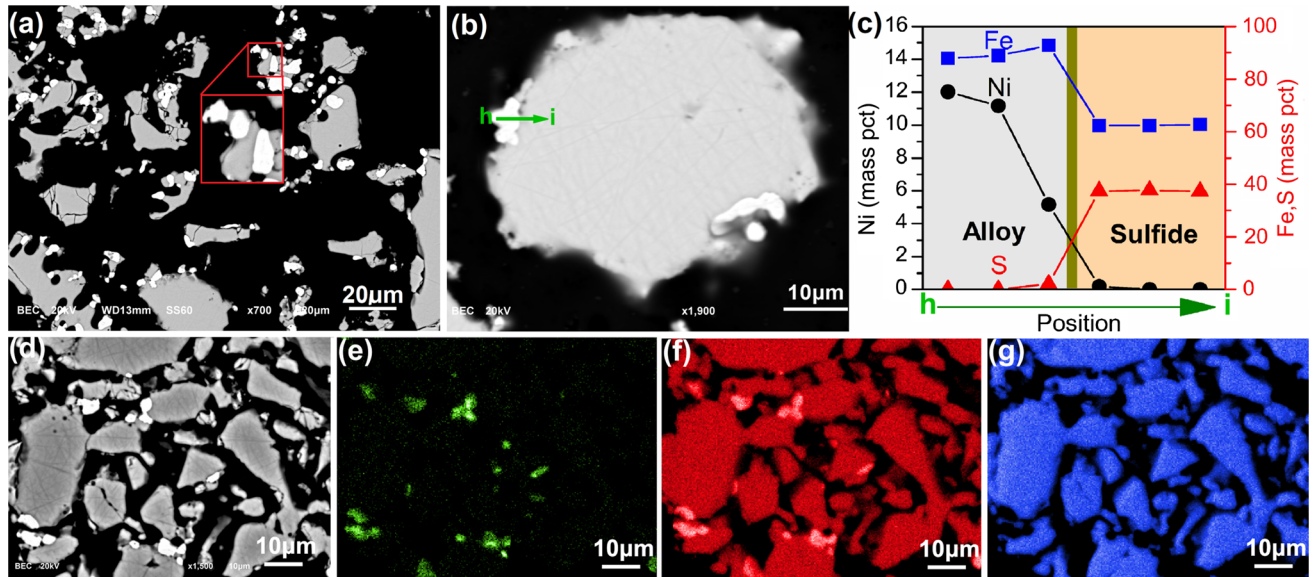


Fig. 9—(a, b) BSE micrographs of the reduced product from Test R2 and (c) EDS point analysis along the arrow h → i; (d) BSE micrograph of the reduced product from Test R3, and its elemental mapping of (e) Ni, (f) Fe, and (g) S.

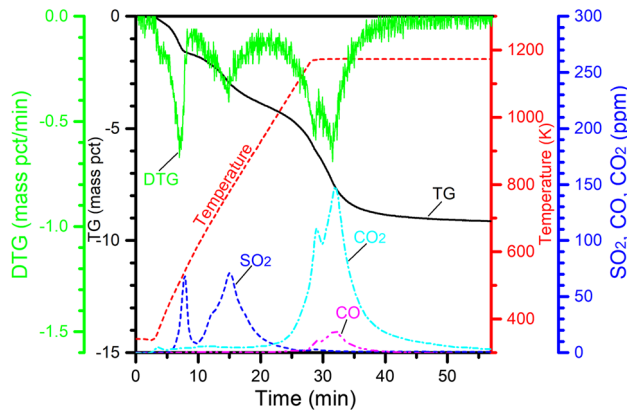
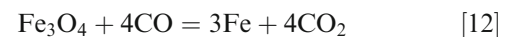
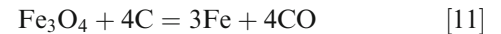
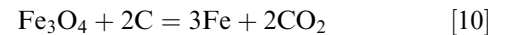


Fig. 10—TG/DTA and offgas analyses on the thermal treatment of pellet fragments composed of Pyrr, magnetite, and petroleum coke (Test T1).

the distribution of Ni between the sulfide and alloy was still not close to equilibrium. The combination of a few factors should have contributed to the deviation from equilibrium. First of all, magnetite and petroleum coke particles must have an initially reasonable contact before magnetite could be reduced directly by petroleum coke (Reactions [10] and [11]). Although it was attempted to provide such conditions by using extremely fine powders and compacting the powders into pellet, solid–solid reactions are still slow due to inadequate contact in atomic scale. The reaction is accelerated in the presence of reducing gases involving the reduction of magnetite by CO (*i.e.*, Reaction [12]) and regeneration of CO by the Boudouard reaction (*i.e.*, Reaction [13]).^[23] However, the Pyrr particles within the pellets act as barriers that hinder the solid and gaseous reduction of Pyrr to a certain degree. For example, Rao^[24] found that the presence of FeS inhibited the reduction of Fe₂O₃ by carbon. It was claimed that the

SO₂ gas generated would compete with CO₂ for available reaction sites on the carbon surface (Reaction [13]), thereby retarding the Boudouard reaction. Resulting from the complex reduction mechanism, nucleation and growth of the metallic Fe particles and their spatial distribution within the sample pellet must allow for effective Ni diffusion from Pyrr particles to their most adjacent Fe particles. Uneven distribution of the newly formed Fe particles within the pellet and their poor physical contact with Pyrr particles would increase the average length of the Ni diffusion path, requiring a longer time for Ni migration into the metallic phase. As seen from Figure 11, the presence of residual petroleum coke particles also acted as a physical barrier to hinder effective Ni diffusion. Due to these factors, dwelling at 1173 K for 30 minutes as shown in Figure 10 was likely not long enough to allow for sufficient extraction of Ni into the metallic phase.



The ferronickel alloy particles formed after the thermal treatment will need to be subsequently physically liberated from their associated sulfide to allow for their separation. As seen from all tests discussed above, essentially most of the alloy particles formed were smaller than 10 μm, imposing a significant challenge in their liberation and subsequent separation. Therefore,

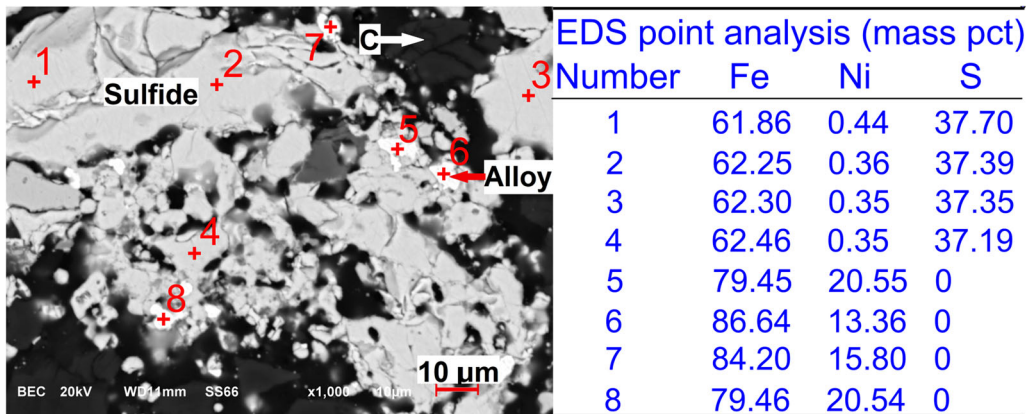


Fig. 11—BSE micrograph of the thermally treated product from Test T1 and EDS point analysis on sulfide and alloy phases.

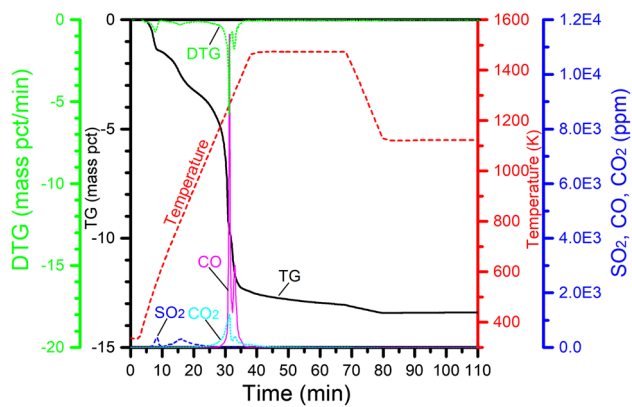


Fig. 12—TG/DTA and offgas analyses on the thermal treatment of the mixture of Pyrr, magnetite, and petroleum coke in an Ar atmosphere (Test T2).

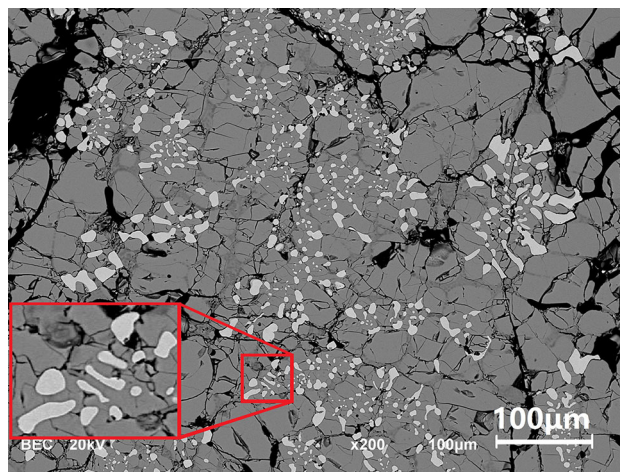


Fig. 13—BSE micrograph of the thermally treated product from Test T2.

growth of the ferronickel alloy is the second focus of the study. One approach was proposed by taking advantage of the thermodynamics as illustrated in Figure 3(b). As seen, temperatures higher than 1373 K would lead to the formation of 100 pct molten matte phase. It can be depicted that the solid γ alloy phase would precipitate from the molten matte upon cooling, during which the growth of the alloy particles is expected. For this purpose, Test T2 (Figure 12) was conducted by heating the mixture (150 mg) of 68.2 mass pct Pyrr, 22.7 mass pct magnetite, and 9.1 mass pct petroleum coke to 1473 K and dwelling for 30 minutes. It was then cooled at a rate of 30 K/min to 1123 K, followed by holding for another 30 minutes to allow for complete solidification of the melt before cooling further to room temperature. As seen, reduction of magnetite (Reactions [10] through [12]) took place resulting in the evolution of CO and CO₂ and its corresponding mass loss, forming metallic Fe. Upon heating to 1473 K, the metallic Fe would be dissolved to form a complete molten matte. Examination of the solidified product (Figure 13) revealed the precipitation of ferronickel alloy particles that were embedded in the sulfide matrix. Quantification

of the size distribution of alloy particles was performed by analyzing the SEM images using the image analysis software ImageJ,^[25] which was plotted in Figure 14. For comparison, the particle size distribution of alloys produced from Test R2 was also plotted. As seen, precipitation of alloys from the molten matte can effectively increase their particle sizes, with a median particle size (*i.e.*, $d(0.5)$) of 13 μm , compared with that of 7 μm for Test R2.

To increase the alloy particle sizes during thermal treatment further, attempts were made by employing a much larger sample size and a slower cooling rate for alloy precipitation. The reason is that a slower cooling rate would allow a longer time for the growth of ferronickel alloy particles in the molten matte. In addition, given a low enough viscosity of the molten matte, the newly formed alloy particles would settle slowly toward the bottom of the melt, due to the density difference between the ferronickel alloy and the molten matte. A slower cooling rate would allow a longer time for the settling of alloy. Further growth of the alloy

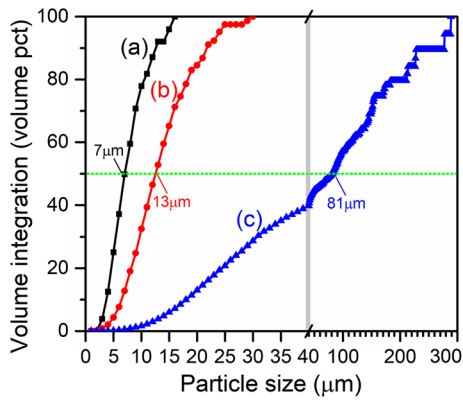


Fig. 14—Size distribution of the alloy particles formed from (a) Test R2, (b) Test T2, and (c) Test T3. (The vertical line indicates the change in the scale of x-axis.)

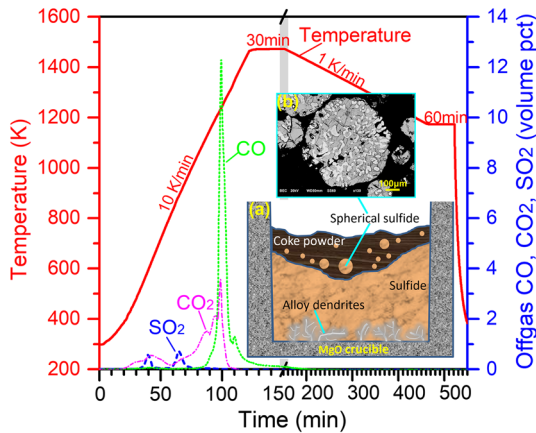


Fig. 15—Temperature profile and offgas analysis in Test T3 (thermal treatment of the mixture of Pyrr, magnetite, and petroleum coke). Inset (a) schematically illustrates the vertical cross section of the product, and (b) BSE micrograph shows the spherical sulfide particles embedded within the petroleum coke powder bed.

particles can be expected at the bottom of the melt due to the presence of a higher population of settled alloy particles that can merge and form larger particles. The population of settled alloy particles can be further increased by using a larger sample size and having a greater depth of the melt. Test T3 was therefore performed by heating 7 g of the mixture of 68.2 mass pct Pyrr, 22.7 mass pct magnetite, and 9.1 mass pct petroleum coke (placed in a MgO crucible, inner diameter 1.5 cm) inside a vertical tube furnace with continuous purging of Ar at 500 mL/min. The temperature profile is plotted in Figure 15 along with the offgas CO, CO₂, and SO₂ concentrations. Similar to Tests T1 and T2, reduction of magnetite by petroleum coke resulted in the evolution of CO and CO₂, forming metallic Fe. On holding at 1473 K for 30 minutes, a complete molten matte would form, followed by slow cooling at a rate of 1 K/min to 1173 K. It was then held at 1173 K for 60 minutes to ensure complete solidification before cooling to room temperature. Figure 15(a) schematically illustrates the vertical cross section of the sample product, measuring a total sample depth of approximately 6 mm. Residual petroleum coke powders in the sample mixture floated to the top after the sulfide became completely molten, during which some sulfide was dragged upward and became entrained and suspended in the petroleum coke powder bed as spherical sulfide particles (Figure 15(b)). As expected, relatively large dendritic alloy particles indeed formed at the bottom of the melt (Figures 15(a) and 16(a) and (b)). This was due to the coalescence of smaller alloy particles that settled to the bottom of melt during slow cooling, as discussed above. Precipitation of smaller alloy particles can be found uniformly throughout the sample cross section, as shown in Figure 16(c). These secondary particles could originate from precipitation just before solidification (so they cannot grow too large) or solid-state diffusion afterward. Likely it is a combination of both of these. The size distribution of the alloy particles

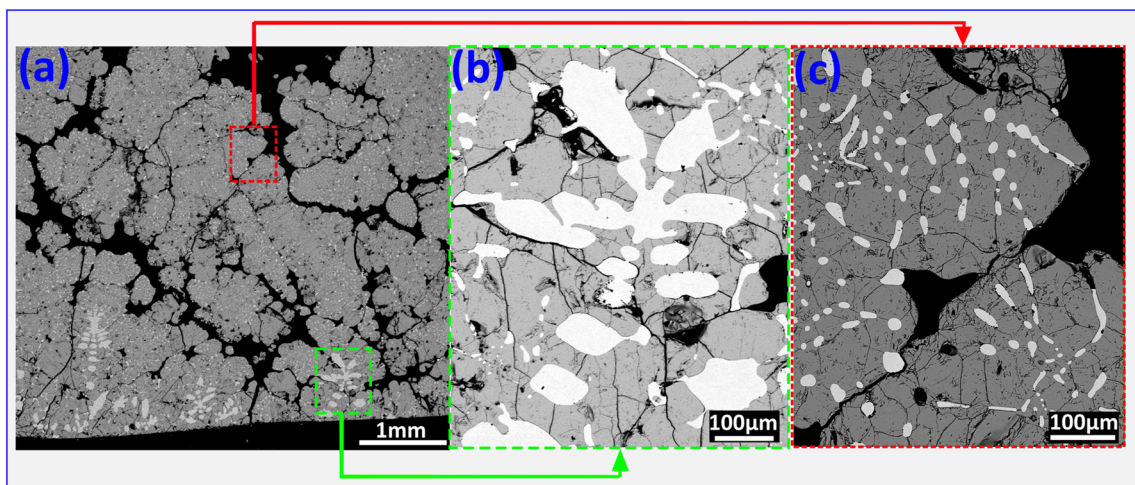


Fig. 16—BSE micrograph (a) of the vertical cross section of the solidified product from Test T3, showing the formation of large dendritic alloy particles (b) at the bottom, and precipitation of smaller alloy particles in other areas (c).

was also analyzed and plotted in Figure 14 for comparison. It is apparent that the growth of ferronickel alloy particles was enhanced significantly, having a median particle size of 81 μm . This demonstrates the effectiveness in promoting alloy growth by the approach of alloy settling, facilitating subsequent liberation of alloys for further upgrading.

IV. CONCLUSION

Thermal upgrading of nickeliferous Pyrr tailings for the recovery of Ni in the form of ferronickel alloy was studied by both thermodynamic evaluation and experimentation. Two thermal upgrading approaches were investigated experimentally: (a) partial oxidation of Pyrr by air for the partial removal of sulfur followed by H_2 reduction; and (b) generation of metallic Fe from the reduction of magnetite by petroleum coke powders that were premixed with Pyrr.

- (1) Thermodynamic assessment demonstrates the possible high Ni recovery in the form of ferronickel alloys at a temperature range of 1073 K to 1173 K by lowering the sulfur-to-metal ratio.
- (2) Study on the oxidation of Pyrr by air revealed the oxidation reactions spanned over a wide temperature range of 413 K to 968 K. The main reaction that led to sulfur removal took place in the temperature range of 653 K to 915 K, forming gaseous SO_2 and hematite ($\alpha\text{-Fe}_2\text{O}_3$) with its characteristic columnar structure. Other side reactions include the formation of FeS_2 at 474 K to 739 K, oxidation of FeS_2 at 739 K to 808 K, formation of sulfates at 739 K to 915 K, etc.
- (3) In the first thermal upgrading approach, both partial oxidation (873 K) and reduction (1173 K) were kinetically fast, taking no more than 25 and 150 seconds, respectively. Ni could be effectively concentrated in the small ferronickel alloy particles ($< 10 \mu\text{m}$) that were intimately attached to the sulfide particles. It was also found that FeS could also be directly reduced by H_2 at 1173 K forming metallic Fe but at a much slower rate.
- (4) In the second thermal upgrading approach, reduction of magnetite by petroleum coke occurred at temperatures above 973 K. Driven by the solubility difference of Ni in metallic Fe vs sulfide phases under thermodynamic equilibrium conditions, diffusion of Ni from the nickeliferous sulfide to the newly formed metallic Fe took place, resulting in the formation of ferronickel alloy with a Ni concentration of 13 to 21 mass pct.
- (5) A sulfur-deficient molten matte phase could form by thermal treatment at a higher temperature of 1473

K. Slow cooling of the molten matte resulted in precipitation and gradual settling of the alloy particles to the bottom of the melt. Relatively large dendritic ferronickel alloy particles could form by recrystallization of the settled alloy particles, thereby significantly increasing the overall alloy particle sizes.

REFERENCES

1. E. Peek, A. Barnes, and A. Tuzun: *Miner. Eng.*, 2011, vol. 24, pp. 625–37.
2. P.F. Wells, S. Kelebek, M.J. Burrows, and D.F. Suarez: In J.A. Finch, S.R. Rao, and I. Holubec (Eds.), In *Proc. UBC-McGill Bi-Annu. Int. Symp. Fundam. Miner. Process.*, Sudbury, Ontario, Canada, 1997, pp. 51–62.
3. S. Garg, K. Judd, R. Mahadevan, E. Edwards, and V.G. Papangelakis: *Can. Metall. Q.*, 2017, vol. 56, pp. 372–81.
4. S. Rezaei, F. Liu, S. Marcuson, M. Muinonen, V.L. Lakshmanan, R. Sridhar, and M. Barati: *Can. Metall. Q.*, 2017, vol. 56, pp. 410–17.
5. L.N. Ertzeva, L.S. Tzemekhman, and V.T. Diachenko: In *Sohn Int. Symp. Adv. Process. Met. Mater. Vol. 8 – Int. Symp. Sulfide Smelt.*, 2006, vol. 8, pp. 419–21.
6. L.N. Ertzeva, L.S. Tzemekhman, and V.T. Diachenko: In *Sohn Int. Symp. Adv. Process. Met. Mater. Vol. 4 – New, Improv. Exist. Technol.: Non-ferr. Mater. Extr. Process.* 2006, vol. 4, pp. 385–87.
7. T. Deng: *Int. J. Miner. Process.*, 1995, vol. 43 (1–2), pp. 91–98.
8. H. Liu: In *EMC '91, Non-ferr. Metall. – Present Future*, 1991, pp. 157–63.
9. J. Gast: *Inco Triangle.*, 1991, vol. 50, p. 5.
10. G. Tremblay: In *Proc. Int. Counc. Met. Environ. (ICME)*, 1998, pp. 32–33.
11. M.R. Gunsinger, C.J. Ptacek, D.W. Blowes, and J.L. Jambor: *J. Contam. Hydrol.*, 2006, vol. 83, pp. 149–70.
12. A. Illis and L.S. Renzoni: Canadian Patent CA155032, 1972.
13. R. Sridhar, A. Dalvi, H.F. Bakker, and A. Illis: *Can. Metall. Q.*, 1976, vol. 15, pp. 255–62.
14. F. Liu, D. Yu, S. Marcuson, F. Wang, B. Li, and M. Barati: *Miner. Eng.*, 2019, vol. 134, pp. 206–14.
15. R. Cameron, B. Yu, C. Baxter, A. Plugatyr, R. Lastra, M. Dalcin, P.H.J. Mercier, and N. Perreault: *Extraction*, 2018, vol. 2018, pp. 2669–79.
16. C.W. Bale, E. Bélisle, P. Chartrand, S.A. Deckerov, G. Eriksson, A.E. Gheribi, K. Hack, I.H. Jung, Y.B. Kang, J. Melançon, A.D. Pelton, S. Petersen, C. Robelin, J. Sangster, P. Spencer, and M.A. Van Ende: *Calphad*, 2016, vol. 54, pp. 35–53.
17. R. Zboril: *Chem. Mater.*, 2002, vol. 14, pp. 969–82.
18. D. Yu and T.A. Utigard: *Thermochim. Acta*, 2012, vol. 533, pp. 56–65.
19. P.G. Thornhill and L.M. Pidgeon: *JOM*, 1957, vol. 9, pp. 989–95.
20. M. Zamalloa and T.A. Utigard: *Can. Metall. Quart.*, 1996, vol. 35, pp. 435–49.
21. D. Yu, M. Zhu, T.A. Utigard, and M. Barati: *Miner. Eng.*, 2013, vol. 54, pp. 32–38.
22. G.J.W. Kor: *Metall. Trans.*, 1974, vol. 5, pp. 339–43.
23. M.O. Boudouard: *Ann. Chim. Phys.*, 1901, vol. 24, pp. 1–85.
24. Y.K. Rao: *Metall. Trans.*, 1971, vol. 2, pp. 1439–47.
25. A.C. Schneider, W.S. Rasband, and K.W. Eliceiri: *Nat. Methods*, 2012, vol. 9, pp. 671–75.

Publisher's Note Springer Nature remains neutral with regard to jurisdictional claims in published maps and institutional affiliations.